

Supporting Information Available

A Combined Theoretical and Mass Spectrometry Study of the Formation-Fragmentation of Small Polyoxomolybdates

Laia Vilà-Nadal,^{a,b} Antonio Rodríguez-Forte,^{*,a} Haralampos N. Miras,^b Elizabeth W. Wilson,^b Leroy Cronin^{*,b} and Josep M. Poblet^{*,a}

Index

1) ESI-MS Solution Preparations	page S2
2) ESI-MS Experimental and Analyses	page S2
(Table S1)	page S3
3) ESI-MS Results Summary (Table S2)	page S4
4) ESI-MS Spectra (Figs. S1-S7)	page S4
5) Car-Parrinello Metadynamics: Parameters	page S11
6) Mo–O rdf for [MoO ₂ (OH) ₂ (H ₂ O) ₂] (Fig. S8)	page S12
7) Mo–O rdf for linear [Mo ₃ O ₁₀] ^{2–} (Fig. S9)	page S13
8) ADF calculations: COSMO methodology	page S14
9) Formation mechanism (M2) Lindqvist anion	page S15
10) Relative energies and figures for optimized structures	page S16
11) Atomic charges and MEP for the lineal trimer [Mo ₃ O ₁₀] ^{2–}	page S22

1) ESI-MS Solution Preparations

$((n\text{-C}_4\text{H}_9)_4\text{N})_2\text{Mo}_6\text{O}_{19}$ Stock Solution: Into 5mL MeCN was dissolved 0.01g of $((n\text{-C}_4\text{H}_9)_4\text{N})_2\text{Mo}_6\text{O}_{19}$.

MS Dilution: An aliquot of 20 μ L of $((n\text{-C}_4\text{H}_9)_4\text{N})_2\text{Mo}_6\text{O}_{19}$ Stock Solution was made up to 4mL with MeCN.

2) ESI-MS Experimental and Analyses

All MS data was collected using a Q-trap, time-of-flight MS (MicroTOF-Q MS) instrument equipped with an electrospray (ESI) source supplied by Bruker Daltonics Ltd. The detector was a time-of-flight, micro-channel plate detector and all data was processed using the Bruker Daltonics Data Analysis 4.0 software, whilst simulated isotope patterns were investigated using Bruker Isotope Pattern software and Molecular Weight Calculator 6.45. The following parameters were consistent for all ESI-MS scans given below. The calibration solution used was Agilent ES tuning mix solution, Recorder No. G2421A, enabling calibration between approximately 100 m/z and 3000 m/z. This solution was diluted 60:1 with acetonitrile. Samples were introduced into the MS *via* direct injection at 180 μ L/h. The electrospray source was used with the drying nitrogen gas temperature at approx +180 °C. The ion polarity for all MS scans recorded was negative, with the end plate offset at -500 V, funnel 1RF at 300 Vpp, funnel 2 RF at 400 Vpp, and hexapole RF at 400 Vpp. The collision cell was filled with argon collision gas. Other MS parameters, and CID (also referred to as MS/MS(MRM), i.e. MS/MS multiple reaction monitoring) parameters, which are set to specific values for each scan, are given in the following table. All theoretical peak assignments were determined via comparison of the experimentally determined isotopic patterns for each peak, with simulated isotopic patterns.

Table S1. MS parameters set to specific values for each scan are presented.

<i>MS Parameter</i>	<i>Data Collection</i>				
	Run A	Run B	Run C	Run D	Run E
Mass Range / m/z	50-3000	50-1500	50-1000	50-2000	50-3000
Capillary / V	4500	4500	4500	4000	3500
Collision Energy / eV	-10	-10	-10	-10	-10
Collision Cell RF / Vpp	500	500	500	500	500
Transfer time / μs	110	110	110	110	110
Pre-pulse Storage Time / μs	10	10	10	10	10
Summation	5000	5000	5000	5000	10000
Time of Acquisition / min	1	1	1	1	1
Active focus	OFF	OFF	ON	ON	ON
Collision cell MS/MS(MRM) parameters	OFF	ON	ON	ON	ON
Peak selected / m/z	-	440.2	440.2	440.2	440.2
Isolation width / m/z	-	20	20	20	20
Collision Energy / eV	-	2	12	16	20

3) ESI-MS Results Summary

Table S2. A summary of the peaks observed from the ESI-MS data collections, along with their associated species are shown.

m/z	Peak Assignment
151.9	$[\text{Mo}_2\text{O}_7]^{2-}$
223.8	$[\text{Mo}_3\text{O}_{10}]^{2-}$
296.8	$[\text{Mo}_4\text{O}_{13}]^{2-}$
368.2	$[\text{Mo}_5\text{O}_{16}]^{2-}$
440.2	$[\text{Mo}_6\text{O}_{19}]^{2-}$

4) ESI-MS Spectra

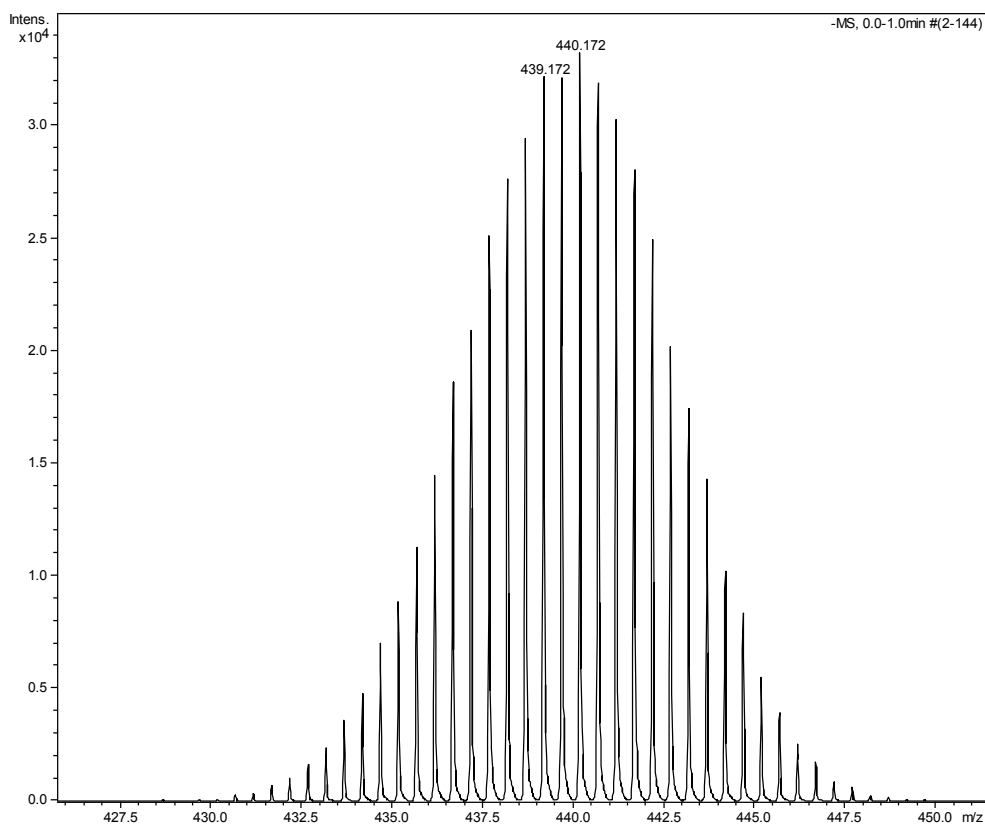


Fig S1 – Mass spectral data from Run A showing the peak associated with the $[\text{Mo}_6\text{O}_{19}]^{2-}$ species at 440.17 m/z.

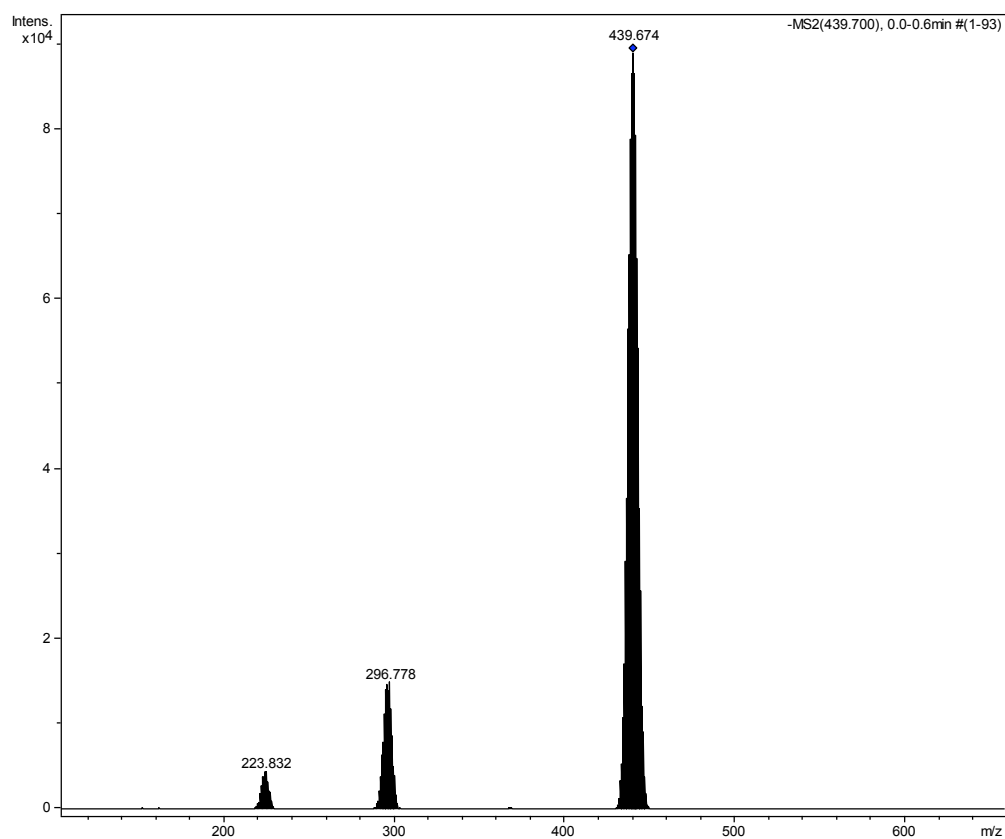


Fig S2 – Mass spectral data from Run B showing the peak associated with the species $[\text{Mo}_6\text{O}_{19}]^{2-}$ at 440.17, $[\text{Mo}_4\text{O}_{13}]^{2-}$ at 296.77 and $[\text{Mo}_3\text{O}_{10}]^{2-}$ at 223.88 m/z respectively.

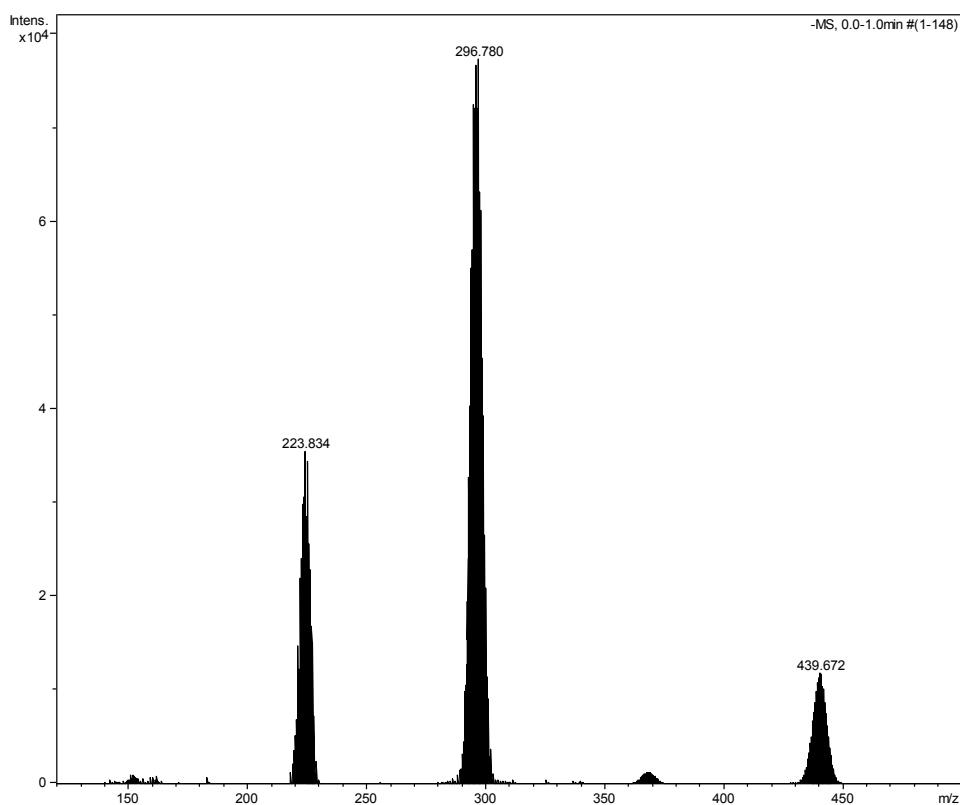


Fig S3 – Mass spectral data from Run E showing the peak associated with the species $[\text{Mo}_6\text{O}_{19}]^{2-}$ at 440.17, $[\text{Mo}_5\text{O}_{16}]^{2-}$ at 368.72, $[\text{Mo}_4\text{O}_{13}]^{2-}$ at 296.77, $[\text{Mo}_3\text{O}_{10}]^{2-}$ at 223.88 and $[\text{Mo}_2\text{O}_7]^{2-}$ at 151.88 m/z respectively.

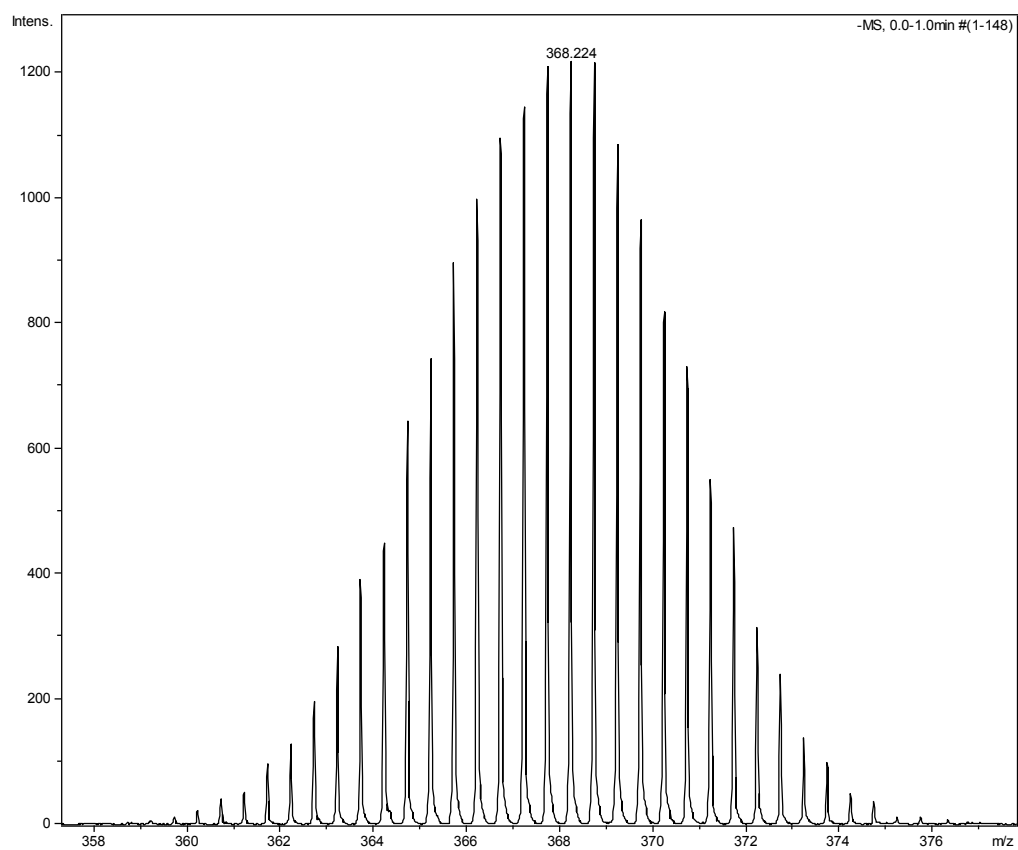


Fig S4 – Mass spectral data from Run E showing the expanded envelope associated with the $[\text{Mo}_5\text{O}_{16}]^{2-}$ species at 368.22 m/z.

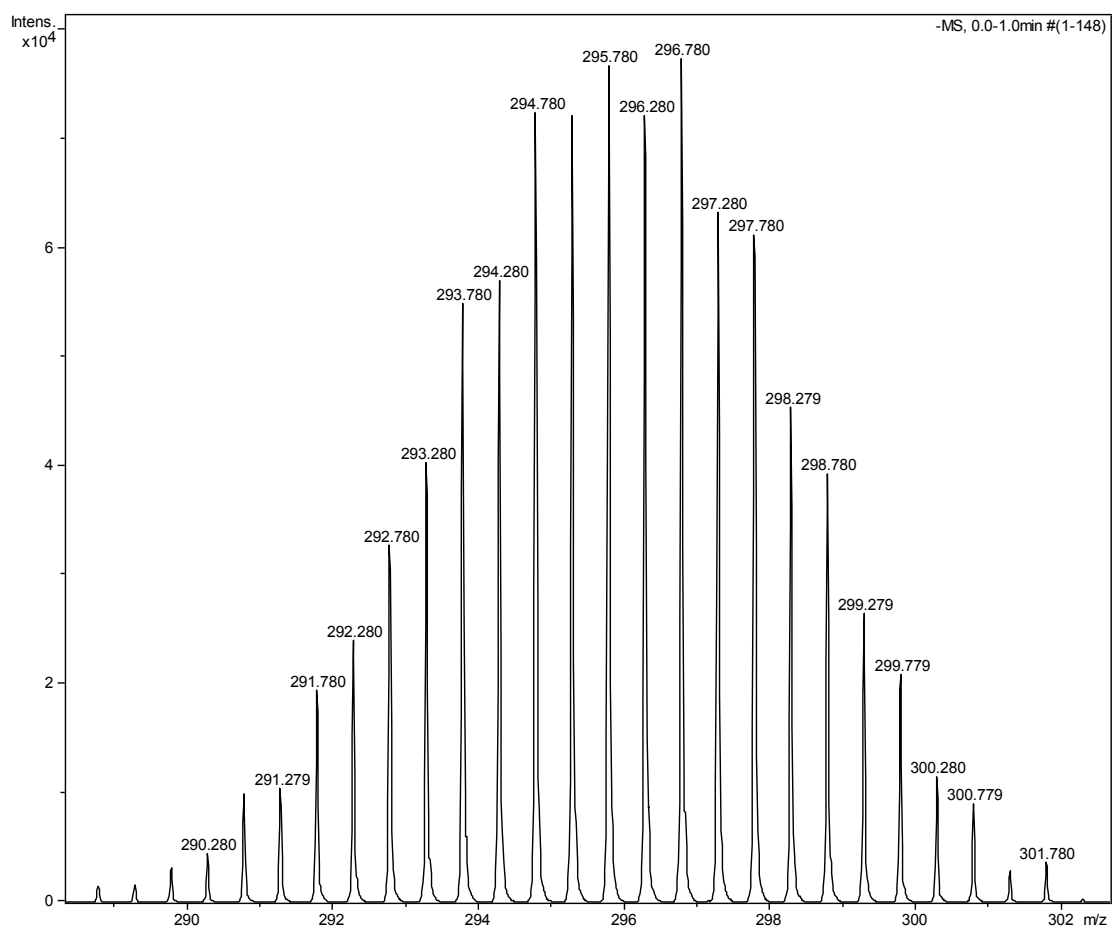


Fig S5 – Mass spectral data from Run E showing the expanded envelope associated with the $[\text{Mo}_4\text{O}_{13}]^{2-}$ species at 296.78 m/z.

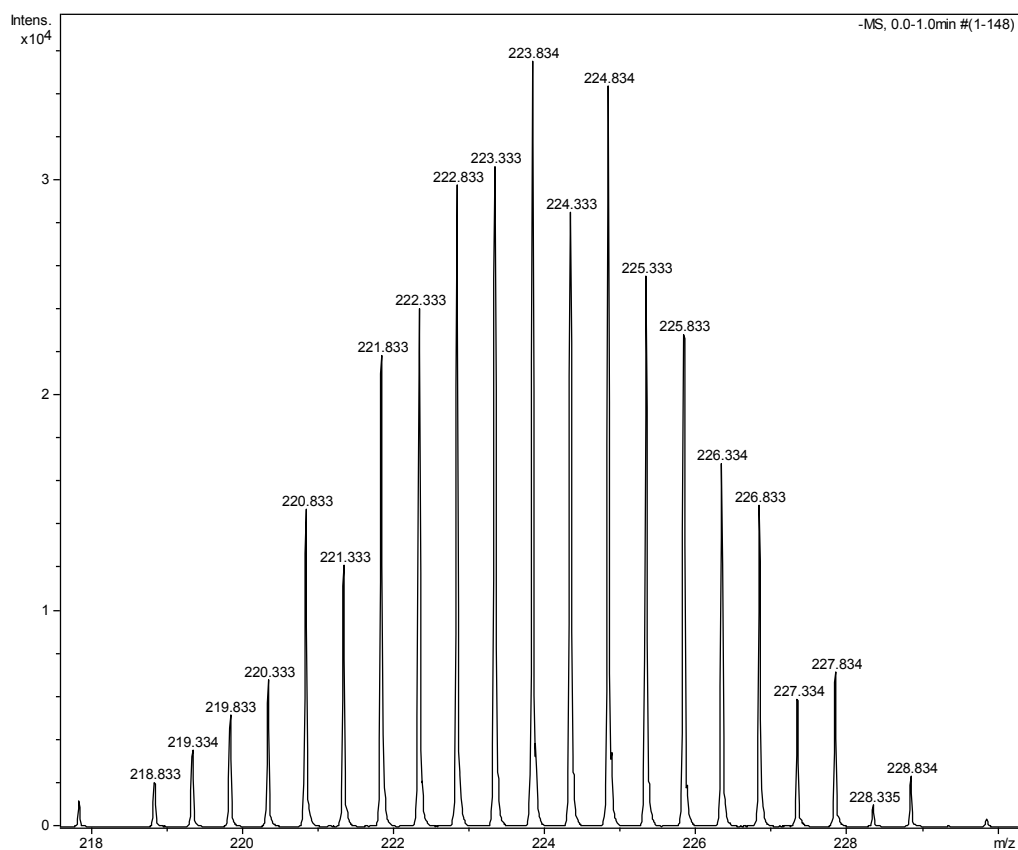


Fig S6 – Mass spectral data from Run E showing the expanded envelope associated with the $[\text{Mo}_3\text{O}_{10}]^{2-}$ species at 223.83 m/z.

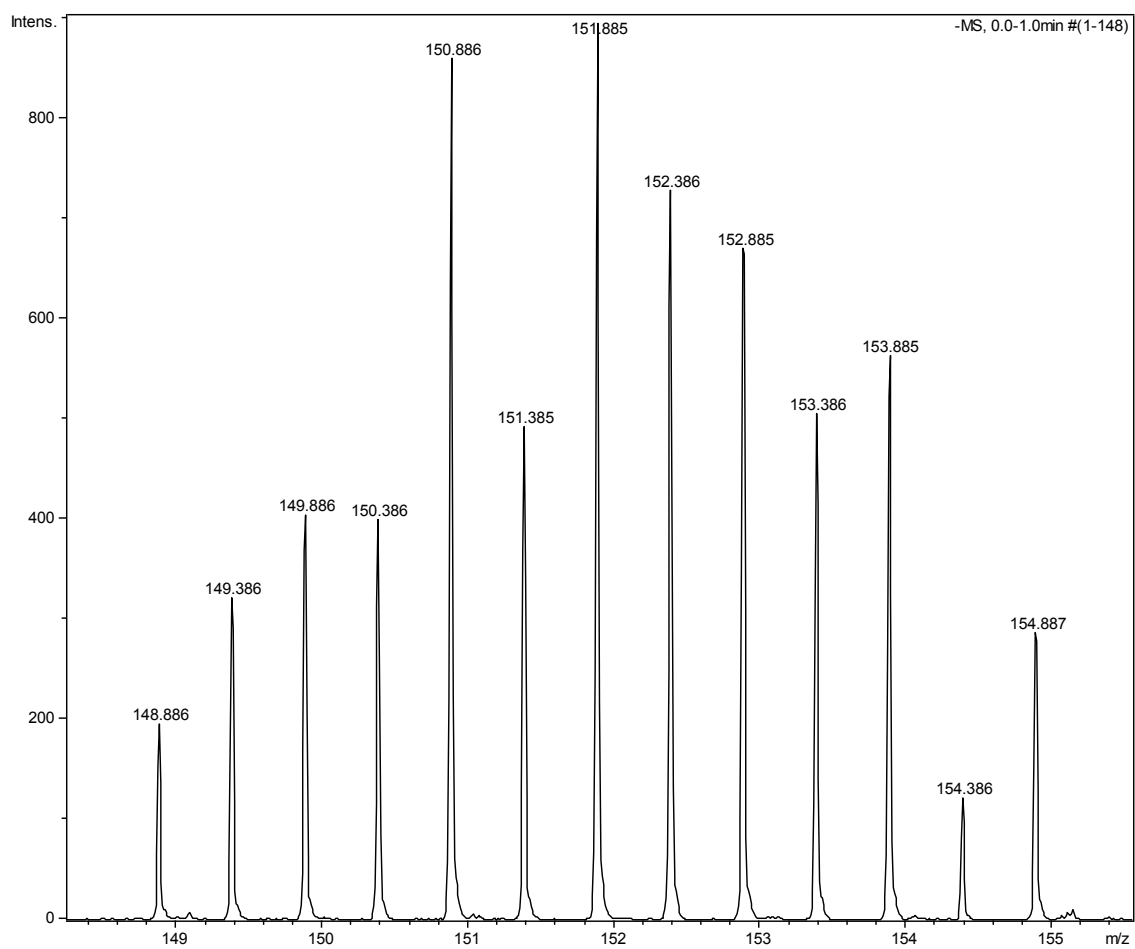


Fig S7 – Mass spectral data from Run E showing the expanded envelope associated with the $[\text{Mo}_2\text{O}_7]^{2-}$ species at 151.88 m/z.

5) Car-Parrinello Metadynamics: Parameters

The CN provides information on the interaction pattern characterizing the actual atomic configuration. Since it is more general and flexible than other order parameters like bond lengths and bond angles, the risk of biasing the reaction on a predetermined path is largely reduced. The analytic definition of the CN of B with respect to A can be found elsewhere.^{30b} In the present work, $p = 8$ and $q = 14$ are used. With this definition, we express the CN as a differentiable curve. As a consequence, the CN of one atom with respect to another is not an integer value (in the present case, around 3.5 when the W ions are four-coordinated and around 4 when they are five-coordinated).

5.1. Hydration of $[\text{MoO}_2(\text{OH})_2]$

In all the metadynamics runs we have chosen as a single collective variable (CV) the distance between the Mo^{VI} ion and the O atom of a nearby water molecule. We have done one simulation for each of the following processes:

- (i) $[\text{MoO}_2(\text{OH})_2] + \text{H}_2\text{O} \rightarrow [\text{MoO}_2(\text{OH})_2(\text{H}_2\text{O})]$
- (ii) $[\text{MoO}_2(\text{OH})_2(\text{H}_2\text{O})] \rightarrow [\text{MoO}_2(\text{OH})_2] + \text{H}_2\text{O}$
- (iii) $[\text{MoO}_2(\text{OH})_2(\text{H}_2\text{O})] + \text{H}_2\text{O} \rightarrow [\text{MoO}_2(\text{OH})_2(\text{H}_2\text{O})_2]$
- (iv) $[\text{MoO}_2(\text{OH})_2(\text{H}_2\text{O})_2] \rightarrow [\text{MoO}_2(\text{OH})_2(\text{H}_2\text{O})] + \text{H}_2\text{O}$

The parameters used for all these runs are: $k = 0.2$ a.u., $M = 10$ a.m.u. The height of the hills (W) is $0.314 \text{ kcal}\cdot\text{mol}^{-1}$, their perpendicular width (Δs^∞) 0.1 a.u., and the deposition rate (Δt) 0.0144 ps. The estimated error (ϵ) in the computation of the free-energy is $1 \text{ kcal}\cdot\text{mol}^{-1}$. The total simulation times (t_{total}) were less than 10 ps.

5.2. Formation of dinuclear species

We have performed three metadynamics runs using the same two CVs: the coordination number (CN) of each Mo atom with respect to the eight O atoms from the MoO_4 groups, $C_{\text{Mo1-O}}$ and $C_{\text{Mo2-O}}$. In the analytic definition of the CN we have used $p = 8$ and $q = 14$. Several parameters are common for the three runs: $k_1 = k_2 = 1.0$ a.u., $\Delta s^\infty = 0.05$ a.u., $\Delta t = 0.0144$ ps. The parameters that change from one simulation to another are:

- (i) $M_1 = M_2 = 10.0$ a.u., $W = 0.188 \text{ kcal}\cdot\text{mol}^{-1}$.
- (ii) $M_1 = M_2 = 30.0$ a.u., $W = 0.126 \text{ kcal}\cdot\text{mol}^{-1}$.
- (ii) $M_1 = M_2 = 40.0$ a.u., $W = 0.126 \text{ kcal}\cdot\text{mol}^{-1}$.

For the three metadynamics, $\epsilon = 0.2 \text{ kcal}\cdot\text{mol}^{-1}$.

6) Mo–O radial distribution function for $[\text{MoO}_2(\text{OH})_2(\text{H}_2\text{O})_2]$

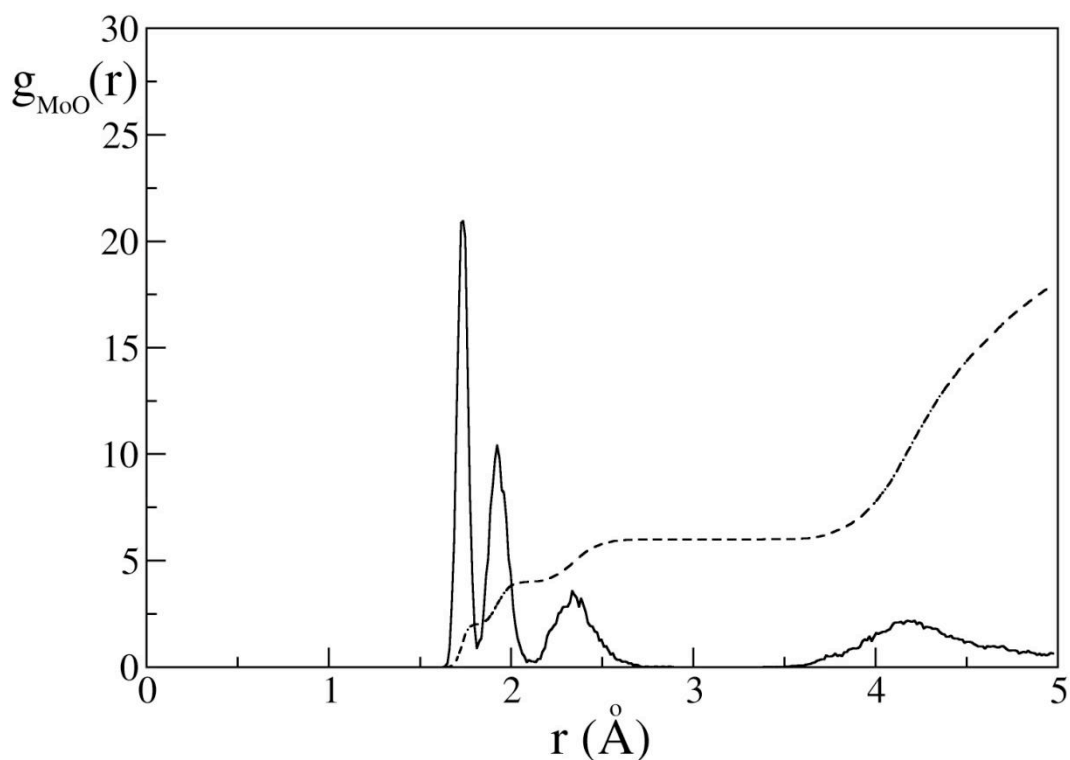


Fig S8 – Mo–O radial distribution function, $g_{\text{MoO}}(r)$ (solid line), and its integration, the coordination number (broken line) for the 29 ps of Car-Parrinello MD simulation of $[\text{MoO}_2(\text{OH})_2(\text{H}_2\text{O})_2]$. The sharp spike at around 1.8 Å, which integrates two O atoms, is attributed to the oxo ligands. The other spike below 2 Å, which integrates two more O atoms, is attributed to the hydroxo ligands. Finally, the spike between 2 and 2.6 Å, which integrates two other O atoms, is due to the aqua ligands coordinated to the Mo^{VI} ion. The coordination number shows a plateau between 2.5 and 3.5 Å associated with the presence of six O atoms in the coordination sphere of the Mo^{VI} ion.

7) Mo–O radial distribution function of central Mo^{VI} ion for linear [Mo₃O₁₀]²⁻

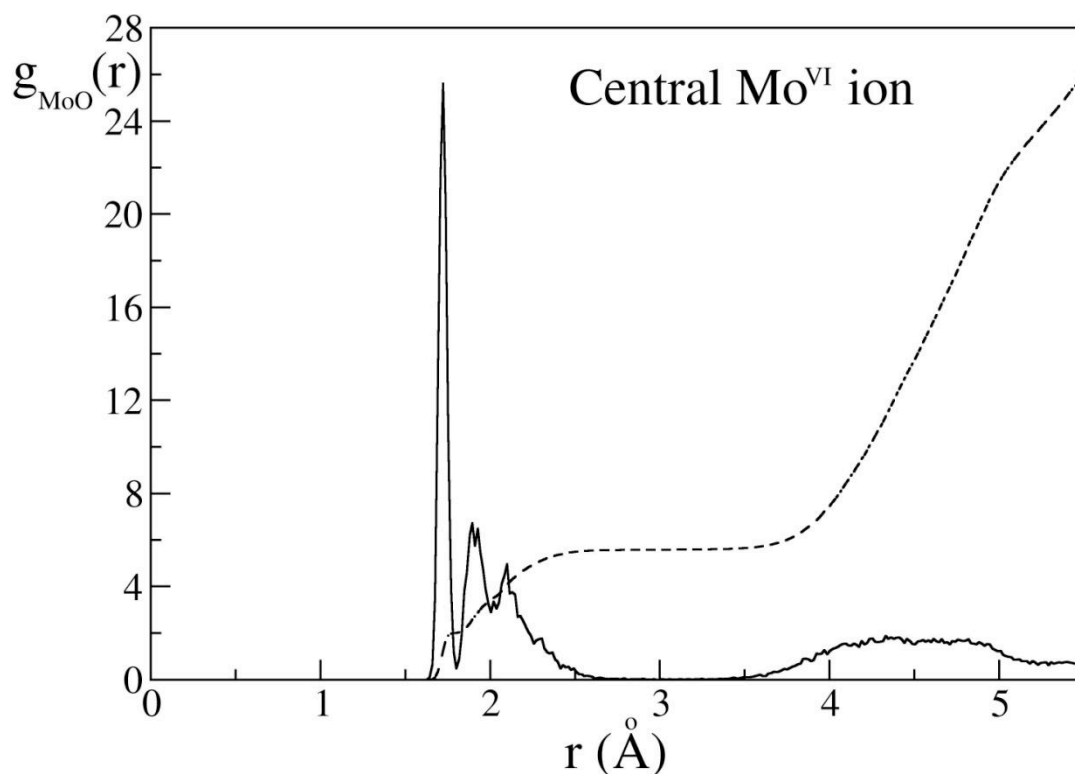


Fig S9 – Mo–O radial distribution function, $g_{\text{MoO}}(r)$ (solid line), and its integration, the coordination number (broken line) of the central Mo^{VI} ion in the linear open-chain [Mo₃O₁₀]²⁻ structure for 14.4 ps of Car-Parrinello MD simulation. The coordination number shows a plateau between 2.5 and 3.5 Å associated with the presence of almost six O atoms in the coordination sphere of the Mo^{VI} ion. At the beginning of the simulation (the first 1.5 ps) the Mo^{VI} ion is tetracoordinated; then, it remains as pentacoordinated for the next 4 ps; and the last 9 ps it stays as hexacoordinated. So, the “average” coordination number for the whole simulation is around 5.5.

8) ADF calculations: COSMO methodology

We have used the Conductor-like Screening Model (COSMO) as implemented in ADF program package. To define the cavity that surrounds the molecules we use the solvent accessible surface (SAS) method and a fine tesserae. Once the geometry has been optimized using the SAS surface, we perform single-point calculations using the solvent excluding surface (SES) that yields more meaningful values for the hydration energies. Geometry optimization using the SES yields “unrealistic” distorted structures when the coordination number of W(VI) ions is lower than six. To obtain the electron density in solution, first it is converged in the gas phase and afterward the COSMO model is turned on to include the solvent effects variationally. The ionic radii of the atoms, which define the dimensions of the cavity surrounding the molecule, are chosen to be 1.26 Å for Mo, 1.52 for O and 1.20 for H. The dielectric constant (ϵ) is set to 78 so as to model water as solvent.

9) Alternative mechanism (M2) for the formation of the Lindqvist anion $[\text{Mo}_6\text{O}_{19}]^{2-}$.

Table S3. Proposed mechanism (M2) for the formation of the Lindqvist anion $[\text{Mo}_6\text{O}_{19}]^{2-}$. ^{a)}

Step		RE	Process type
1	$[\text{MoO}_3(\text{OH})]_{(\text{aq})}^- + [\text{MoO}_3(\text{OH})]_{(\text{aq})}^- \rightarrow [\text{Mo}_2\text{O}_6(\text{OH})_2]_{(\text{aq})}^{2-}$	0.4	Aggregation
2	$[\text{Mo}_2\text{O}_6(\text{OH})_2]_{(\text{aq})}^{2-} + \text{H}_3\text{O}^+_{(\text{aq})} \rightarrow [\text{Mo}_2\text{O}_6(\text{OH})]_{(\text{aq})}^- + 2\text{H}_2\text{O}_{(\text{aq})}$	-18.3	Water condensation
3	$[\text{Mo}_2\text{O}_6(\text{OH})]_{(\text{aq})}^- + [\text{MoO}_3(\text{OH})]_{(\text{aq})}^- \rightarrow [\text{Mo}_3\text{O}_9(\text{OH})_2]_{(\text{aq})}^{2-}$	-1.7	Aggregation
4	$[\text{Mo}_3\text{O}_9(\text{OH})_2]_{(\text{aq})}^{2-} + \text{H}_3\text{O}^+_{(\text{aq})} \rightarrow [\text{Mo}_3\text{O}_9(\text{OH})]_{(\text{aq})}^- + 2\text{H}_2\text{O}_{(\text{aq})}$	-6.7	Water condensation
5	$[\text{Mo}_3\text{O}_9(\text{OH})]_{(\text{aq})}^- + [\text{MoO}_3(\text{OH})]_{(\text{aq})}^- \rightarrow [\text{Mo}_4\text{O}_{12}(\text{OH})_2]_{(\text{aq})}^{2-}$	-10.2	Aggregation
6	$[\text{Mo}_4\text{O}_{12}(\text{OH})_2]_{(\text{aq})}^{2-} + \text{H}_3\text{O}^+_{(\text{aq})} \rightarrow [\text{Mo}_4\text{O}_{12}(\text{OH})]_{(\text{aq})}^- + 2\text{H}_2\text{O}_{(\text{aq})}$	-17.2	Water condensation
7	$[\text{Mo}_4\text{O}_{12}(\text{OH})]_{(\text{aq})}^- + [\text{MoO}_3(\text{OH})]_{(\text{aq})}^- \rightarrow [\text{Mo}_5\text{O}_{15}(\text{OH})_2]_{(\text{aq})}^{2-}$	16.9	Aggregation
8	$[\text{Mo}_5\text{O}_{15}(\text{OH})_2]_{(\text{aq})}^{2-} + \text{H}_3\text{O}^+_{(\text{aq})} \rightarrow [\text{Mo}_5\text{O}_{15}(\text{OH})]_{(\text{aq})}^- + 2\text{H}_2\text{O}_{(\text{aq})}$	-3.5	Water condensation
9	$[\text{Mo}_5\text{O}_{15}(\text{OH})]_{(\text{aq})}^- + [\text{MoO}_3(\text{OH})]_{(\text{aq})}^- \rightarrow [\text{Mo}_6\text{O}_{18}(\text{OH})_2]_{(\text{aq})}^{2-}$	-14.3	Aggregation
10	$[\text{Mo}_6\text{O}_{18}(\text{OH})_2]_{(\text{aq})}^{2-} \rightarrow [\text{Mo}_6\text{O}_{19}]_{(\text{aq})}^{2-} + \text{H}_2\text{O}_{(\text{aq})}$	-12.3	Water condensation

^{a)} Reaction energies (RE) are in kcal mol⁻¹.

10) Tables with the computed relative energies and figures for the optimized structures analyzed in this work.

Table S4. Relative energies (in kcal mol⁻¹) with respect to the lowest-energy species for trinuclear clusters.

Structure			ΔE (kcal mol ⁻¹)
[Mo ₃ O ₁₀] ²⁻	1	tr-3	0.0
	2	tr-4	+4.8
	3		+7.9
	4		+15.4
	5	tr-5	+19.4
	6		+49.5
[Mo ₃ O ₉ (OH)] ⁻	1		+1.0
	2		0.0
	3		+8.6
	4		+12.7
	5		+18.0
	6		+38.6
[Mo ₃ O ₁₀ (OH)] ³⁻	1	tr-1	0.0
	2		+2.12
	3		-
	4	tr-2	+0.5
[Mo ₃ O ₉ (OH) ₂] ²⁻	1		+2.1
	2		0.0
	3		+0.9
	4		+1.2

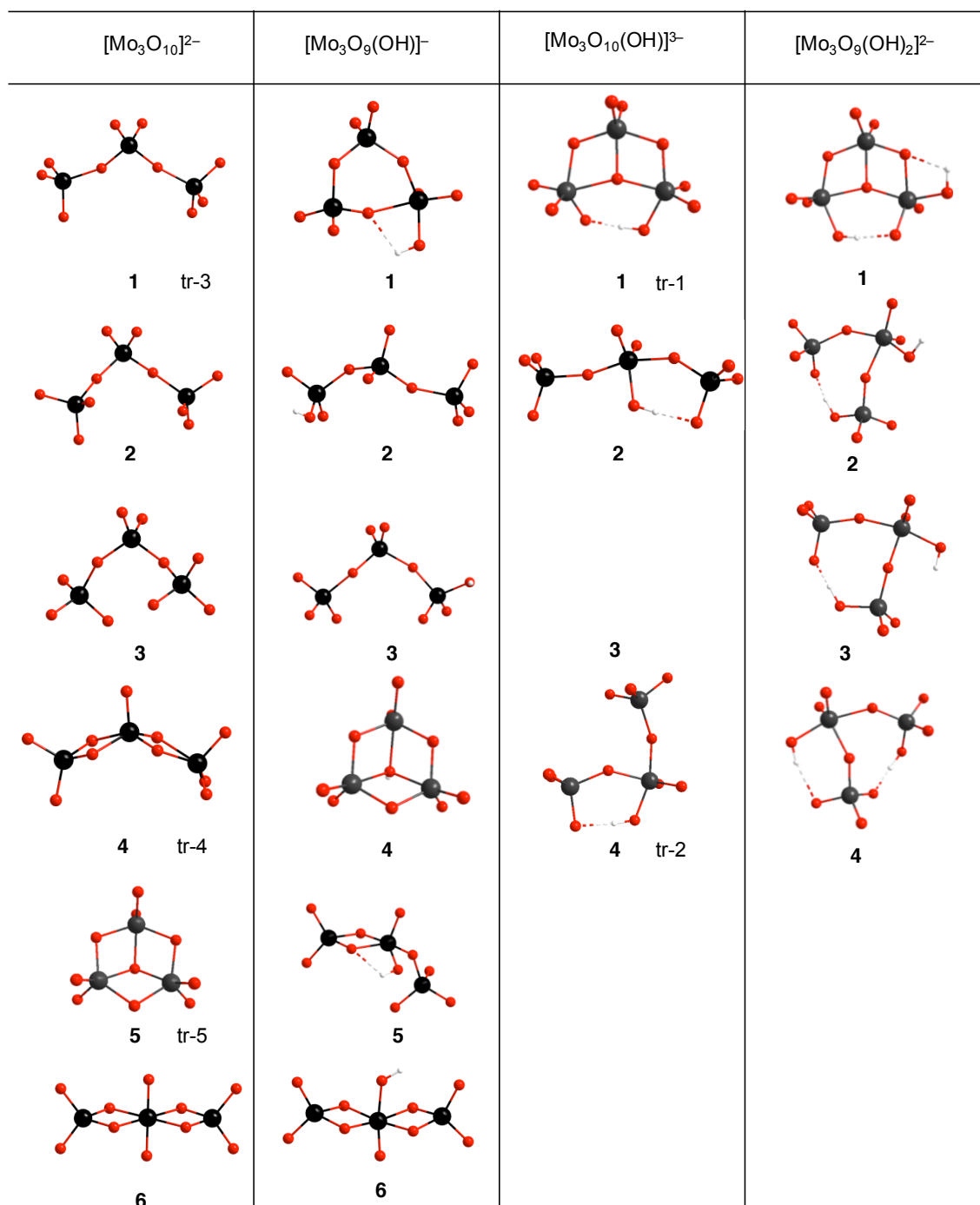


Fig S10 – Ball-and-stick representations for the optimized structures of the trinuclear species with $[\text{Mo}_3\text{O}_{10}]^{2-}$, $[\text{Mo}_3\text{O}_9(\text{OH})]^-$, $[\text{Mo}_3\text{O}_{10}(\text{OH})]^{3-}$ and $[\text{Mo}_3\text{O}_9(\text{OH})_2]^{2-}$ stoichiometries.

Table S5. Relative energies (in kcal mol⁻¹) with respect to the lowest-energy species for tetranuclear clusters.

Structure		ΔE (kcal mol ⁻¹)	
[Mo ₄ O ₁₃] ²⁻	1	te-4	0.0
	2	te-5	+3.6
	3		+3.9
	4		+9.5
[Mo ₄ O ₁₂ (OH)] ⁻	1		0.0
	2		+3.6
	3		+8.3
	4		+10.2
	5		+10.6
[Mo ₄ O ₁₃ (OH)] ³⁻	1		+7.1
	2	te-1	0.0
	3	te-2	+1.1
	4	te-3	+5.5
	5		+7.5
[Mo ₄ O ₁₂ (OH) ₂] ²⁻	1		0.0
	2		+4.3
	3		+2.3
	4		+7.2
	5		+6.3
	6		+10.7
	7		+12.3

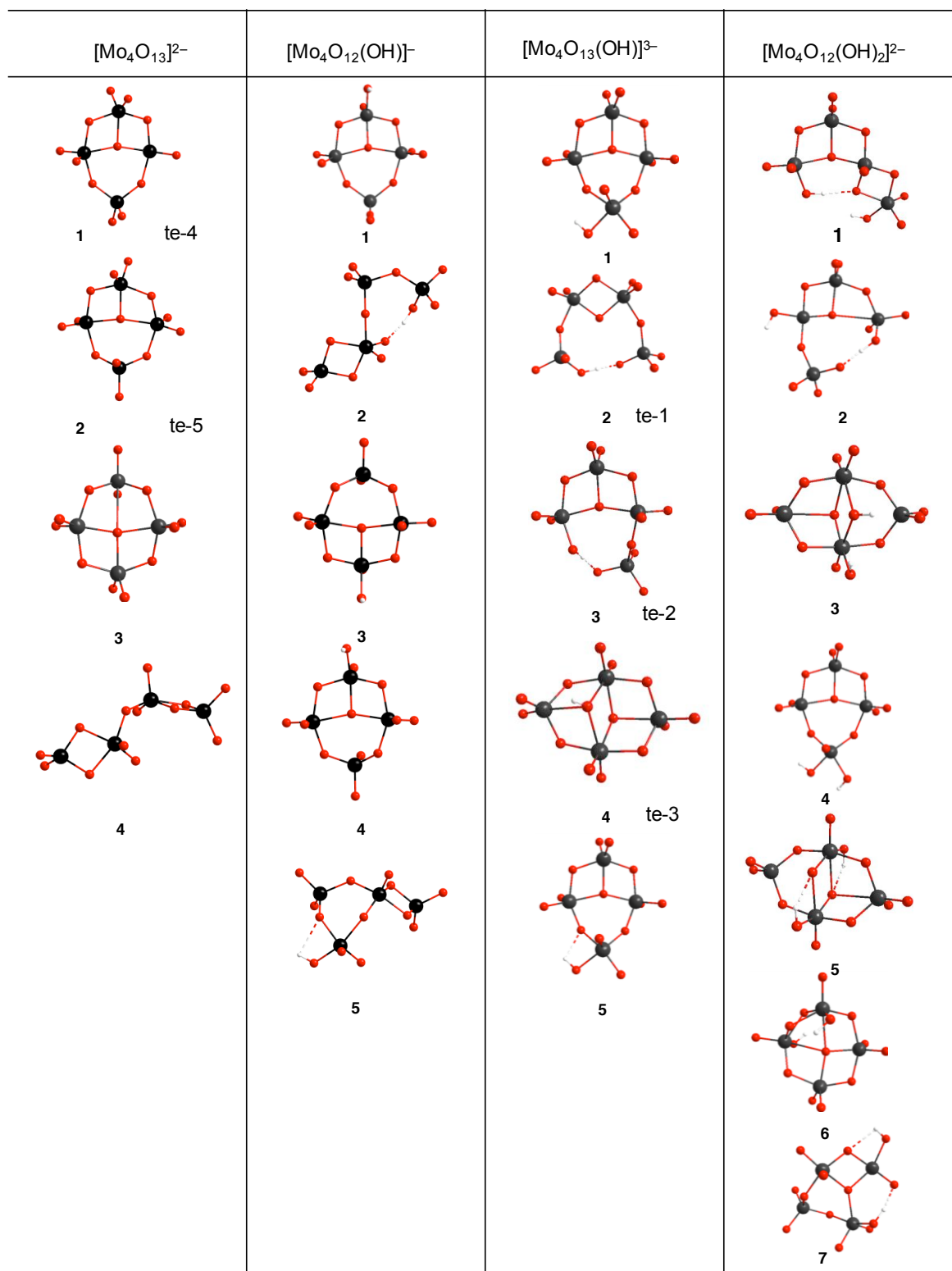


Fig S11 – Ball-and-stick representations for the optimized structures of the tetranuclear species with $[\text{Mo}_4\text{O}_{13}]^{2-}$, $[\text{Mo}_4\text{O}_{12}(\text{OH})]^-$, $[\text{Mo}_4\text{O}_{13}(\text{OH})]^{3-}$ and $[\text{Mo}_4\text{O}_{12}(\text{OH})_2]^{2-}$ stoichiometries.

Table S6. Relative energies (in kcal mol⁻¹) with respect to the lowest-energy species for pentanuclear clusters.

Structure		ΔE (kcal mol ⁻¹)	
[Mo ₅ O ₁₆] ²⁻	1	pe-3	0.0
	2		+2.6
	3		+3.6
	4	pe-4	+1.0
	5		+9.8
[Mo ₅ O ₁₅ (OH)] ⁻	1		0.0
	2		+2.5
	3		+1.2
	4		+20.7
	5		+1.5
[Mo ₅ O ₁₆ (OH)] ³⁻	1	pe-1	+1.2
	2		-
	3	pe-3	+3.4
	4		+4.7
	5		0.0
	6		+0.1
[Mo ₅ O ₁₅ (OH) ₂] ²⁻	1		+4.0
	2		0.0
	3		+1.8
	4		+2.4
	5		+8.5
	6		+11.3

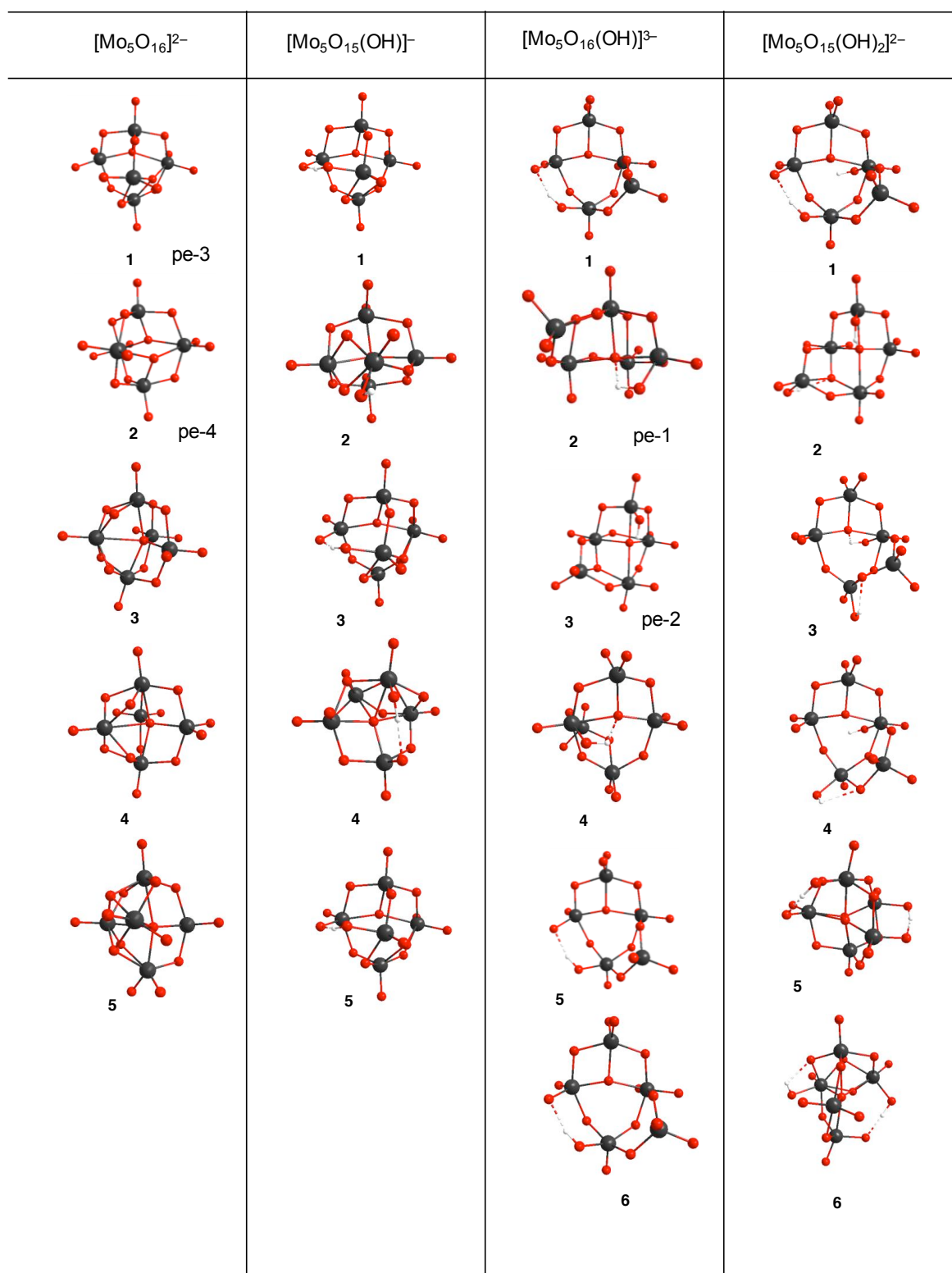


Fig S11 – Ball-and-stick representations for the optimized structures of the pentanuclear species with $[\text{Mo}_5\text{O}_{16}]^{2-}$, $[\text{Mo}_5\text{O}_{15}(\text{OH})]^-$, $[\text{Mo}_5\text{O}_{16}(\text{OH})]^{3-}$ and $[\text{Mo}_5\text{O}_{15}(\text{OH})_2]^{2-}$ stoichiometries.

Table S7. Relative energies (in kcal mol⁻¹) with respect to the monomers for hexanucler clusters.

Structure		ΔE (kcal mol ⁻¹)	
$[\text{Mo}_6\text{O}_{19}]^{2-}$	1	he-1	-66.9
$[\text{Mo}_6\text{O}_{19}(\text{OH})]^{3-}$	2	he-2	-35.1
$[\text{Mo}_6\text{O}_{18}(\text{OH})_2]^{2-}$	3		-54.5

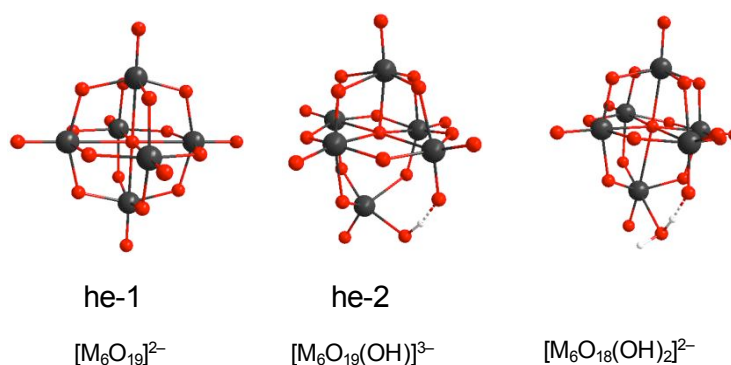


Fig S12 – Ball-and-stick representations for the optimized structures corresponding to $[\text{Mo}_6\text{O}_{19}(\text{OH})]^{3-}$ and $[\text{Mo}_6\text{O}_{18}(\text{OH})_2]^{2-}$ stoichiometries and the Lindqvist anion $[\text{Mo}_6\text{O}_{19}]^{2-}$.

11) Atomic charges and MEP for the lineal trimer $[\text{Mo}_3\text{O}_{10}]^{2-}$

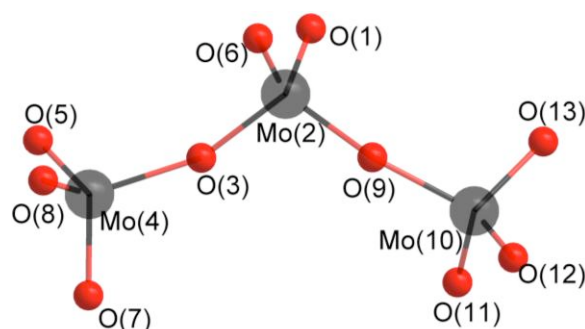


Fig S13 – Labelled ball-and-stick representation of the optimized structure for the $[\text{Mo}_3\text{O}_{10}]^{2-}$ lineal trimer.

Table S8. Atomic charges according to different partition schemes.

Atoms		OPT asurf			SP esurf			Gas phase		
		Mull ^a	Hirsh ^b	VDD ^c	Mull ^a	Hirsh ^b	VDD ^c	Mull ^a	Hirsh ^b	VDD ^c
1	O	-0.7255	-0.3759	-0.393	-0.7938	-0.4075	-0.420	-0.7286	-0.3784	-0.396
2	Mo	2.1554	0.7738	0.793	2.3626	0.8706	0.861	2.1633	0.7813	0.799
3	O	-0.9987	-0.3684	-0.335	-1.0109	-0.3514	-0.301	-0.9962	-0.3676	-0.331
4	Mo	1.9755	0.6705	0.756	2.2080	0.7599	0.827	1.9854	0.6782	0.762
5	O	-0.7771	-0.4382	-0.475	-0.8625	-0.4801	-0.512	-0.7813	-0.4416	-0.479
6	O	-0.7236	-0.3757	-0.394	-0.7911	-0.4046	-0.417	-0.7327	-0.3838	-0.403
7	O	-0.7757	-0.4374	-0.475	-0.8601	-0.4782	-0.512	-0.7767	-0.4373	-0.474
8	O	-0.7788	-0.4387	-0.475	-0.8623	-0.4791	-0.511	-0.7837	-0.4427	-0.479
9	O	-0.9986	-0.3701	-0.339	-1.0146	-0.3556	-0.310	-0.9971	-0.3699	-0.335
10	Mo	1.9753	0.6717	0.756	2.1936	0.7536	0.821	1.9844	0.6800	0.763
11	O	-0.7766	-0.4360	-0.471	-0.8556	-0.4751	-0.506	-0.7730	-0.4335	-0.468
12	O	-0.7746	-0.4336	-0.469	-0.8542	-0.4734	-0.506	-0.7790	-0.4368	-0.472
13	O	-0.7769	-0.4410	-0.479	-0.8589	-0.4792	-0.512	-0.7847	-0.4472	-0.487

^{a)} Mulliken Populations; ^{b)} Hirshfeld charge analysis; ^{c)} Voronoi deformation density (VDD)

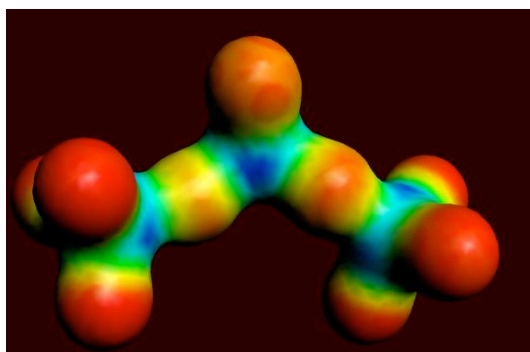


Fig S14 –Molecular electrostatic potential map for linear $[\text{Mo}_3\text{O}_{10}]^{2-}$. Blue identifies regions where the electrostatic potential is more positive (electrophilic regions). Red identifies regions where the electrostatic potential is more negative (nucleophilic regions)